Supporting information

Lithiophilic Interlayer Driven 'Bottom-up' Metal Infilling in High Current Density Li-Metal Anodes

*Syed Abdul Ahad[1], Janina Drews[2,3], Timo Danner[2,3], Arnulf Latz[2,3,4], Hugh Geaney[1] **

[1]Department of Chemical Sciences and Bernal Institute, University of Limerick, Limerick, V94 T9PX, Ireland

[2]Institute of Engineering Thermodynamics, German Aerospace Center (DLR), Wilhelm-Runge-Straße 10, 89081 Ulm, Germany

[3]Helmholtz Institute Ulm (HIU), Helmholtzstr.11, 89081 Ulm, Germany

[4]Institute of Electrochemistry, Ulm University (UUlm), Albert-Einstein-Allee 47, 89081 Ulm, Germany

E-mail: hugh.geaney@ul.ie

Continuum model and parameterization

- Butler-Volmer equation, which correlates the Faradaic current density across the electrode-electrolyte interface i_{se} with the overpotential η:

$$i_{se} = i_0 \cdot \left[\exp\left(\frac{F}{RT}(1-\alpha)\eta\right) - \exp\left(\frac{F}{RT}\alpha\eta\right)\right] \quad \text{(S1)}$$

- Exchange current density i_0:

$$i_0 = F \cdot k_{BV} \cdot c_e^{1-\alpha} \cdot c_{Li}^{\alpha} \quad \text{(S2)}$$

$$0 = -\vec{\nabla}\vec{j}_{e,eff} = \vec{\nabla}\left(\varepsilon_e^{\beta}\kappa \cdot \vec{\nabla}\varphi_e\right) + \vec{\nabla}\left(\varepsilon_e^{\beta}\kappa \cdot \frac{t_+ - 1}{F}\frac{RT}{c_e} f_{thermo}\vec{\nabla}c_e\right) \quad \text{(S3)}$$

- Charge conservation in the electrolyte:

- Mass conservation in the electrolyte:

$$\frac{\partial \varepsilon_e c_e}{\partial t} = -\nabla \vec{N}_{e,eff} = \vec{\nabla}\left(\varepsilon_e^{\beta} D_e \cdot \vec{\nabla} c_e\right) - \vec{\nabla}\left(\frac{t_+}{F} \vec{j}_{e,eff}\right) \tag{S4}$$

$$0 = -\vec{\nabla} \vec{j}_s = \vec{\nabla}\left(\sigma \cdot \vec{\nabla} \Phi_s\right) \tag{S5}$$

- Charge conservation in the electrode:

Model extensions in 1D:

- Change of Li volume fraction

$$\frac{\partial \varepsilon_{Li}}{\partial t} = -\frac{M_{Li}}{\rho_{Li}} \cdot a \cdot \frac{i_{se}}{F} \tag{S6}$$

- Specific surface area for Li plating with two contributions (plating on the uncovered surface of the host structure and plating on the surface of existing Li deposits):

$$a = a_0 \cdot (1 - \Theta) + a_0 \cdot \left(\frac{\varepsilon_{Li}}{\varepsilon_{Li,ref}}\right)\left(\frac{\varepsilon_{e,}}{\varepsilon_{e,0}}\right)^{1,5} \tag{S7}$$

  Note, that Equation (S7) is an empirical expression based on the approach of Richter et al..[17] In general, the surface area of the host material decreases with ε_{Li} until it is fully covered with Li, while the available surface of the Li deposits increases during initial plating, but decreases later on due to pore clogging.

- Effective Li volume fraction $\varepsilon_{Li,eff}$ (mean between the values for ε_{Li} of the control volume ix and its direct neighbors of all three dimensions) to enable propagation of Li growth between the control volumes of the spatial discretization.

$$\varepsilon_{Li,eff} = \frac{5\varepsilon_{Li(ix)} + \varepsilon_{Li(ix-1)} + \varepsilon_{Li(ix+1)}}{7} \tag{S8}$$

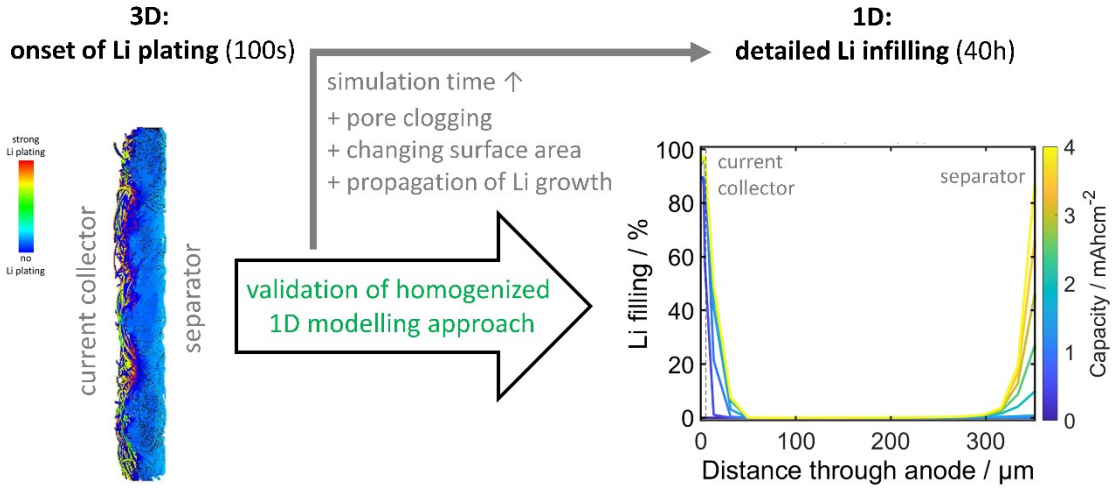

Figure S1. Schematic overview of interplay between simulations on 3D and 1D level.

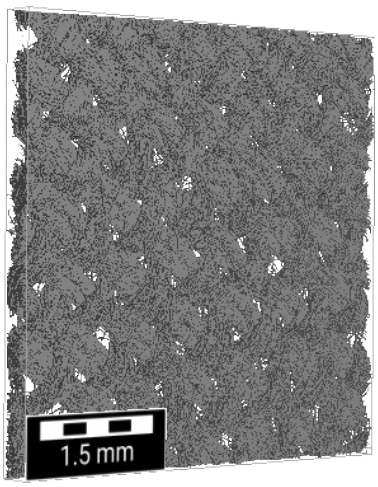

Figure S2. Microstructure of the CC measured by micro-CT with a resolution of 5µm.

Geometric parameter	Value
Celgard 2325 Separator	
Porosity ε_e	0.39
Bruggeman coefficient β	4
Thickness	25µm
1071 HCB CC Anode	
Porosity $\varepsilon_{e,0}$	0.5
Bruggeman coefficient β	2
Thickness	356µm
Specific surface area a_0	242 m^2/m^3
Ge interlayer	
Porosity $\varepsilon_{e,0}$	0.5
Bruggeman coefficient β	2
Thickness	5µm
Specific surface area a_0	484 m^2/m^3

Table S1. Geometric parameters of separator and anode for simulation of Li plating in a half cell.

Electrolyte parameter	Value	Reference
Initial concentration c_e	1.25 mol/L	
Conductivity κ	1.1 S/m	2
Diffusion coefficient D	$5 \cdot 10^{-10}$ m^2/s	3
Transference number $t+$	0.5	3
Thermodynamic factor f_{thermo}	1	

Table S2. Transport parameters of the LiTFSI + $LiNO_3$ in DOL/DME (1:1) electrolyte.

Kinetic parameter	Value	Reference
Rate constant k_{BV}	$2.5 \cdot 10^{-7}$ m/s	4
Symmetry factor α	0.5	
Open-circuit potential U_0 (vs. Li/Li^+)	0V	
$\varepsilon_{Li,ref}$	$5 \cdot 10^{-4}$	
$n_{Li,ref}$	$8 \cdot 10^{-13}$ mol	
Nucleation overpotential on CC $\eta_{nuc(CC)}$	0- 0.1V	
Nucleation overpotential on Ge $\eta_{nuc(Ge)}$	0V	5

Table S3. Kinetic parameters of Li plating on CC and Ge.

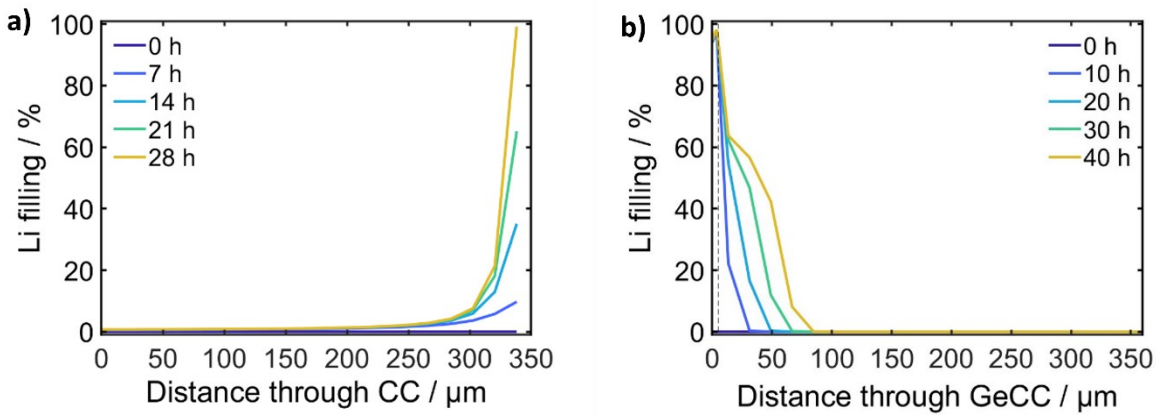

Figure S3. 1D continuum simulations: Temporal evolution of the infilling of (a) CC and (b) GeCC with plated Li at 0.1 mAcm^{-2} ($\eta_{nuc(CC)}$=20 mV). The current collector is located at x = 0 µm, while the separator is beginning at the end of the x-axis.

Microscopic plating morphology $\varepsilon_{Li,ref}$

The reference volume fraction of Li $\varepsilon_{Li,ref}$ at which the surface of the host material is fully covered by plated Li, indicated whether the metal deposition is rather smooth or uneven. The theoretical minimum value of $\varepsilon_{Li,ref}$ is given by the specific surface area of the host material a_0 and the radius of atomic Li r_{Li} (Equation (S9)), meaning that the host structure is covered by one perfect monolayer (ML) of Li.

$$\varepsilon_{Li,ref} \geq \varepsilon_{Li,ref}^{ML} = a_0 \cdot 2r_{Li} \approx 7.4 \cdot 10^{-8} \quad \text{(S9)}$$

However, in reality Li plating will occur via nucleation and growth. Thereby, the critical size of a Li nuclei will be much larger than a Li atom, typically in the range of few nm ($r_{Li,crit} \approx$ 1-3nm, depending on the current density).[6] Consequently, the more realistic minimum value of $\varepsilon_{Li,ref}$ for perfectly smooth Li deposition is in the range of $3-7 \cdot 10^{-7}$ which corresponds to approximately 3-10 ML of Li metal (Equation (S9)). Practically, it can be assumed that even for relatively smooth Li deposition the value of $\varepsilon_{Li,ref}$ will be significantly higher since it is very unlikely that the electrode surface gets completely covered by Li nuclei of the critical size. Instead growth will play a role as well. As a result, even for a $\varepsilon_{Li,ref}$ that is a few orders of magnitude higher than its minimum value the plating morphology can still be considered to be very smooth. Unfortunately, it is challenging to study the microscopic morphology evolution during Li deposition. Therefore, the value for the model parameter $\varepsilon_{Li,ref}$ will remain a rough estimate. To study the impact of $\varepsilon_{Li,ref}$ a parameter study is carried out and it is found that the $\varepsilon_{Li,ref}$ mainly determines the maximum filling of the CC pores with Li. (**Figure S3**). Since the SEM analysis implies a quite dense Li infilling of the CC (**Figure 4**), a value in the range of 10^{-5}-10^{-4} (≈ 100-1000 ML Li) overall seems to be a reasonable estimation for $\varepsilon_{Li,ref}$ (Table S3). It is also found, that the influence of $\varepsilon_{Li,ref}$ on the general plating mechanism (top-down vs. bottom-up) is neglectable (**Figure S3**) and therefore the exact value of $\varepsilon_{Li,ref}$ is not crucial for the simulation results. Only for very low $\varepsilon_{Li,ref}$, close to the absolute minimum value, the filling mechanism changes from bottom-up filling to on-top plating. However, such a low value for $\varepsilon_{Li,ref}$ would imply a perfect layer-by-layer growth, which is not very likely.

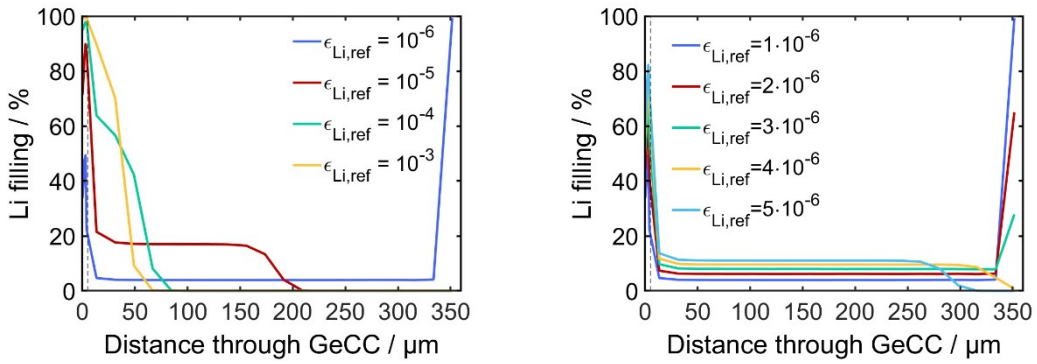

Figure S4. 1D continuum simulations: Influence of $\varepsilon_{Li,ref}$ on the infilling of GeCC with plated Li after 4 mAhcm^{-2} at 0.1 mAcm^{-2} ($\eta_{nuc(CC)}$=20 mV). The Ge interlayer is positioned at 0-5 µm and is facing towards the current collector.

For the 3D simulations based on the model of Hein et al.[7] the value of $\varepsilon_{Li,ref}$ is converted into a molar quantity of Li metal $n_{Li,ref}$. Following their approach, the value for 1 ML $n_{Li,ref}^{ML}$ can be calculated based on the voxel size of the microstructure (5 µm), the atomic radius of Li and its molar volume (Equation (S10)) which directly correlates to the previously determined value of $\varepsilon_{Li,ref}^{ML}$ (Equation (S9)).

$$n_{Li,ref}^{ML} = (5\ \mu m)^2 \cdot 2r_{Li} \cdot \frac{\rho_{Li}}{M_{Li}} = 5.8 \cdot 10^{-16}\ \text{mol} \qquad \text{(S10)}$$

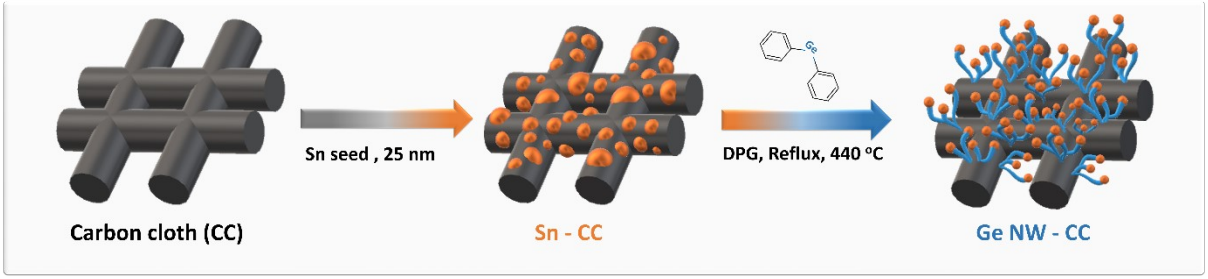

Figure S5. Figure S1. Schematic illustration representing steps towards the synthesis of Ge NWs decorated on CC (GeCC).

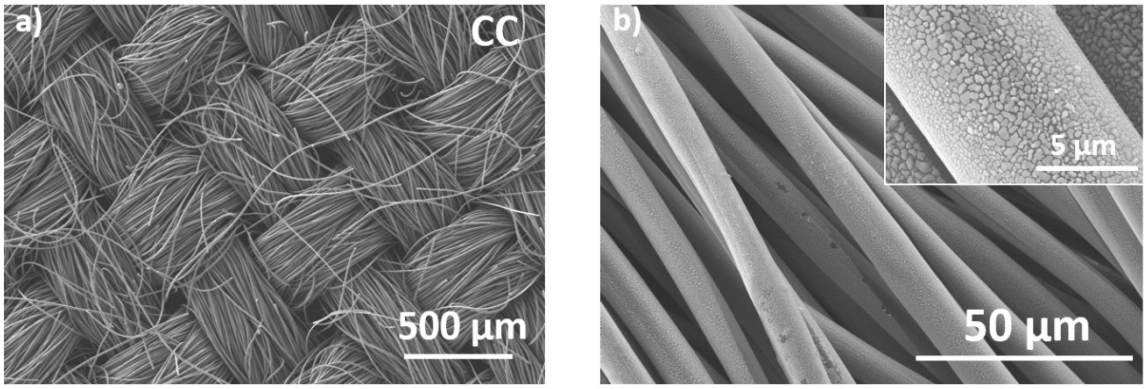

Figure S6. SEM images of (a) CC and (b) Sn coated CC. (Inset: high magnification image of Sn coated CC fiber)

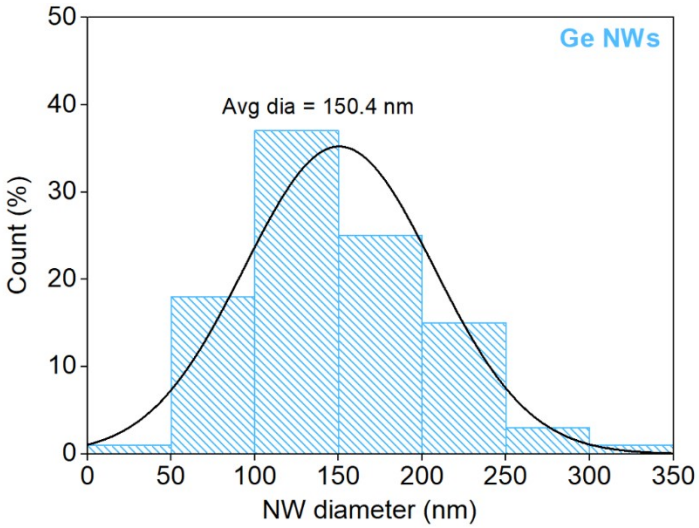

Figure S7. Histogram representing diameter distribution of Ge NWs. The average diameter of Ge NWs was 150.4 nm.

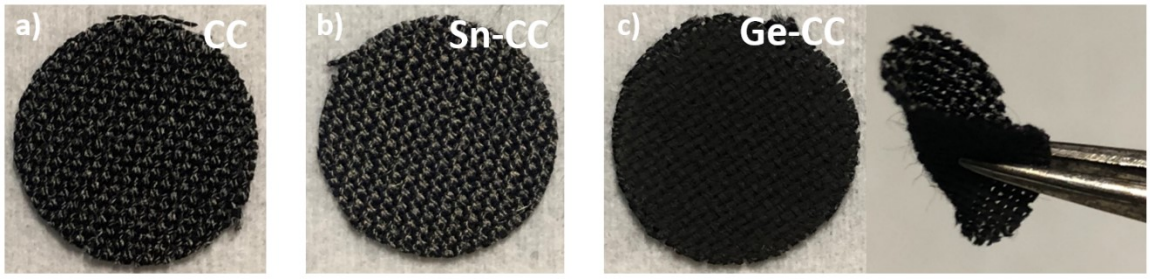

Figure S8. Photographic images of (a) CC, (b) Sn-CC after Sn thermal evaporation and (c) GeCC after Ge NWs growth on Sn-CC substrate. The image also shows high flexibility of GeCC substrate.

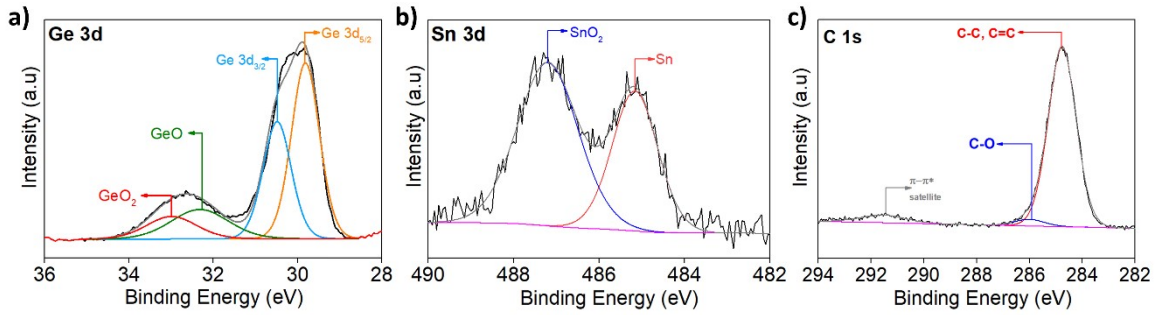

Figure S9. XPS analysis of GeCC interlayer representing core-level spectra of (a) Ge 3d, (b) Sn 3d, and (c) C 1s.

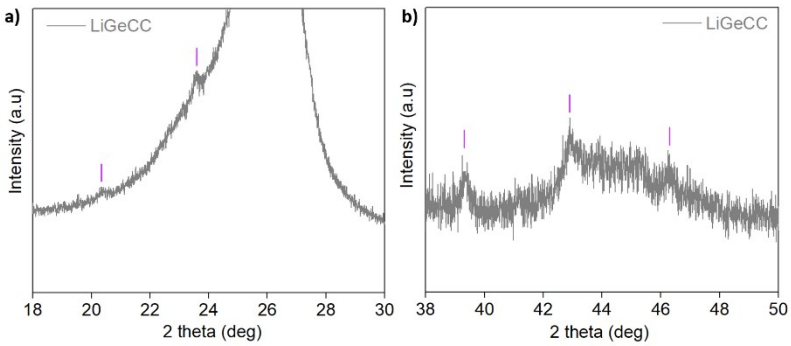

Figure S10. Segmented XRD analysis of GeCC interlayer between (a) 18°-30° and (b) 38°-40° to represent major $Li_{15}Ge_4$ peaks appearing after lithiation using short-circuiting method.

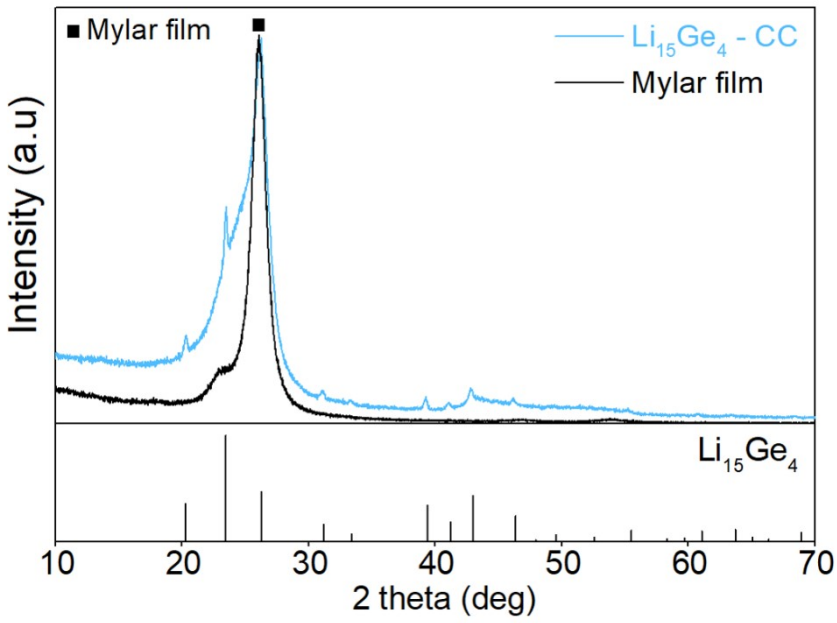

Figure S11. XRD analysis of lithiated GeCC showcasing formation of $Li_{15}Ge_4$ after short-circuiting method.

For the XRD analysis, lithiated GeCC was removed from the underlying Li foil to enhance the signals generated from $Li_{15}Ge_4$ phase. A background spectrum of Mylar film has also been included which was used to protect sample from oxidation in air.

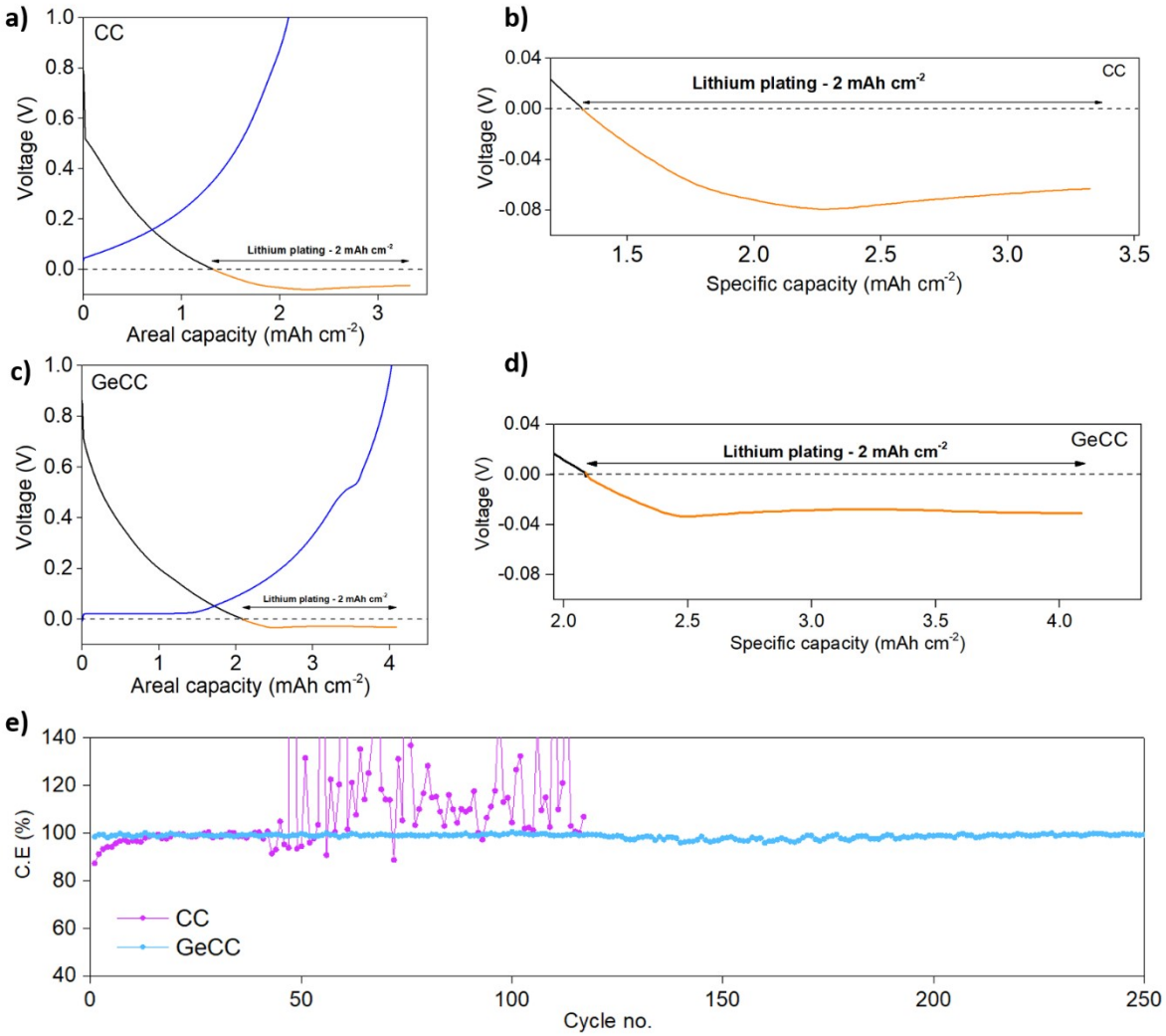

Figure S12. 1st cycle voltage-specific capacity profile of (a, b) CC and (c, d) GeCC cycled at 2 mA cm^{-2}, 2mAh cm^{-2}. (e) Columbic efficiency vs. cycle no. plot of CC and GeCC vs. Li at 2 mA cm^{-2}, 2 mAh cm^{-2}. The delithiation voltage was set at 1.0 V.

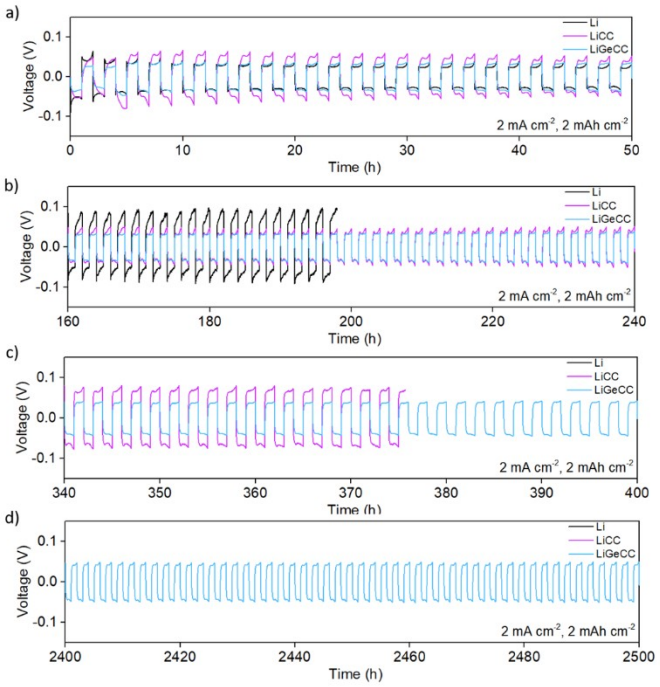

Figure S13. The voltage-time graph of Li, LiCC and LiGeCC at various time frames of (a) 0-50h , (b) 160-240 h, (c) 340-400 h, (d) 2400-2500 h.

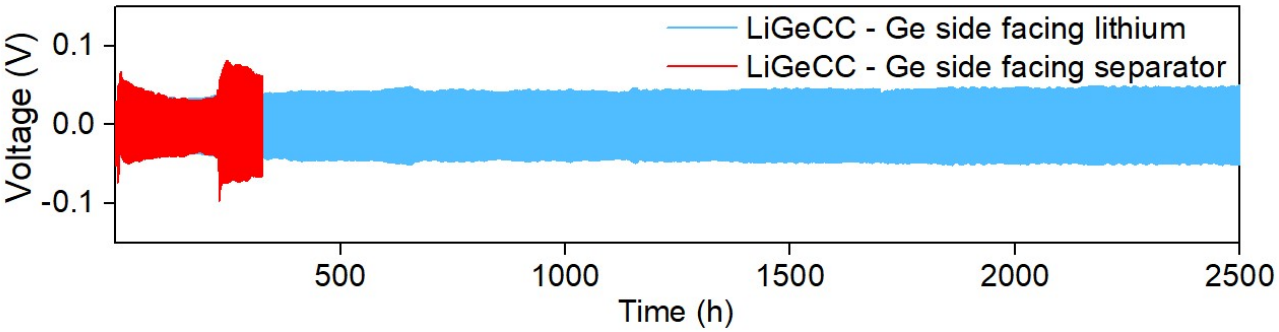

Figure S14. Comparison of symmetric cell cycling with LiGeCC (Ge side facing lithium) and LiGeCC (Ge side facing separator) at 2 mA cm^{-2}, 2mAh cm^{-2}.

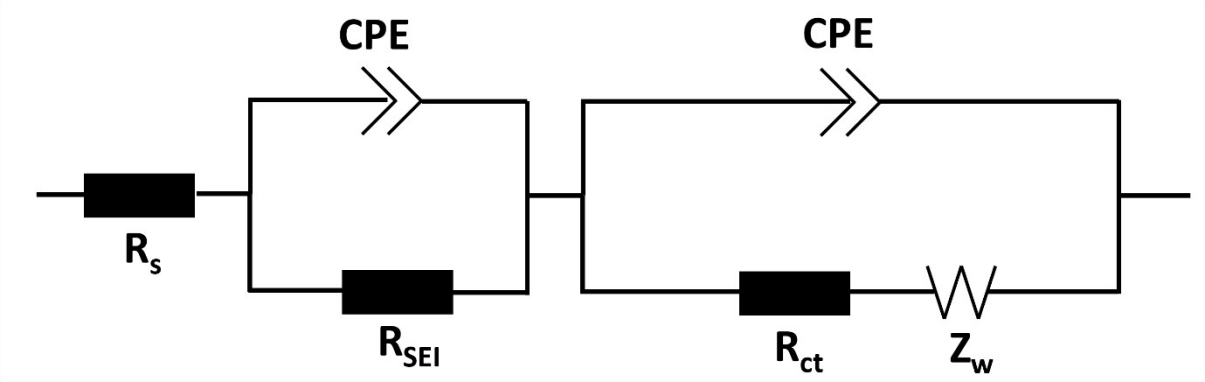

Figure S15. The equivalent circuit used to calculate Rs, R_{SEI} and R_{ct}. Rs is the ohmic resistance of the cell, Rct is the charge transfer resistance, CPE is the capacitance while Z_w is the Warburg factor.

Sample	Cycle no.	R_s (Ohm)	R_{SEI} (Ohm)	R_{ct} (Ohm)	R_{SEI+ct} (Ohm)
Li	1st	6.2	15.2	26.5	**41.7**
	100th	7.0	18.6	26.6	**45.2**
LiCC	1st	5.9	13.6	22.6	**36.2**
	100th	7.2	14.6	23.2	**37.8**
LiGeCC	1st	6.1	6.9	8.5	**15.4**
	100th	7.1	3.1	5.6	**8.7**

Table S4. Table representing Rs, RSEI, Rct and total cell internal cell resistance (R_{SEI}+R_{ct}).

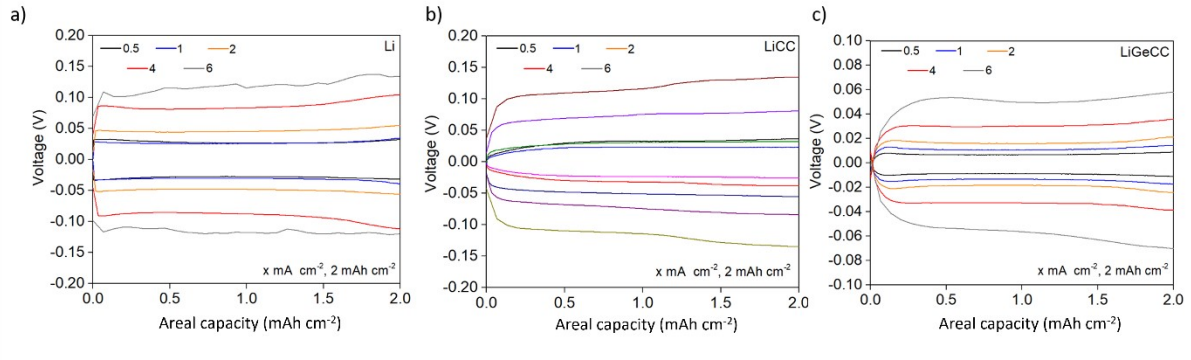

Figure S16. A comparison of the voltage vs. Areal capacity graphs of (a) Li, (b) LiCC and (c) LiGeCC at various current densities with fixed current density of 2 mA cm^{-2}.

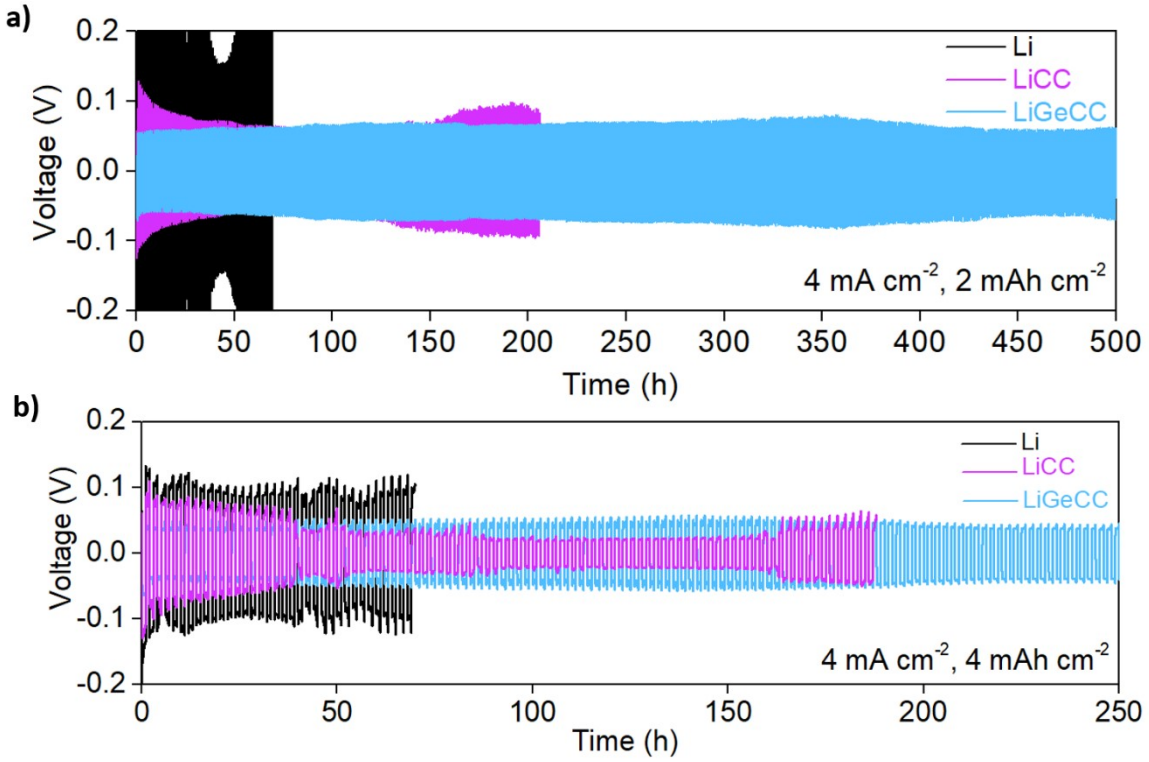

Figure S17. Symmetric cell performance of Li, LiCC and LiGeCC anodes at (a) 4mA cm^{-2}, 2mAh cm^{-2} and (b) 4 mA cm^{-2}, 4 mAh cm^{-2}.

	Metal anode interlayers	Current density (mA cm^{-2})	Areal capacity (mAh cm^{-2})	Hours (h)	Ref.
1	CNTs	1	1	200 h	8
2	Ni mesh	1	1	~1400 h	9
		3	1	~650	
3	Stainless steel mesh	1	1	250 h	10
		5	1	250 h	
4	Copper mesh	0.5	1	1280 h	11
		1	1	600 h	
		2	1	120 h	
5	Carbon cloth	1	1	400 h	12
		3	1	~140 h	
		5	1	~100 h	
6	Coiled glass fiber	1	1	~1000 h	13
		2	1	270 h	
		5	1	150 h	
7	Mullite fiber	2	1	~1000 h	14
8	GZCNT (CNT-ZnO interlayer)	1	1	1040 h	15
		5	1	~120 h	
		10	1	~100 h	
9	Gr10 (Gradient coating of polymer, Zn ions)	1	1	Over 2000 h	16
		6	1	100 h	
		4	2	180 h	
10	SFC/CNTs	2	2	600 h	17
		5	2	200 h	
11	**GeCC**	**2**	**2**	**2500 h**	**This work**
		2	**4**	**1000 h**	
		4	**2**	**500 h**	
		4	**4**	**250 h**	

Table S5. Comparison of the current density vs. plating capacity w.r.t to the life span of symmetric cells with previously published studies based on interlayer/ Li metal anode.

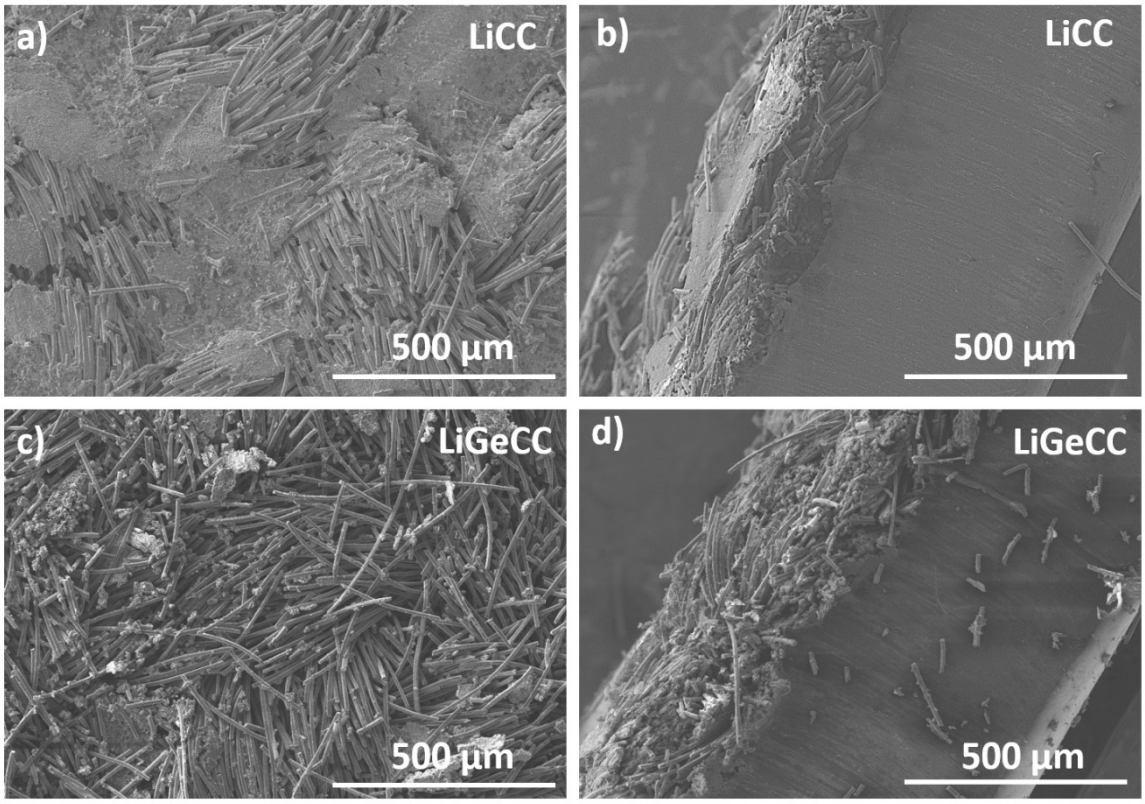

Figure S18. SEM analysis of (a, b) LiCC and (c, d) LiGeCC anodes after 100 cycles at 2 mA cm^{-2}, 2mAh cm^{-2}. The anodes were examined after the stripping step.

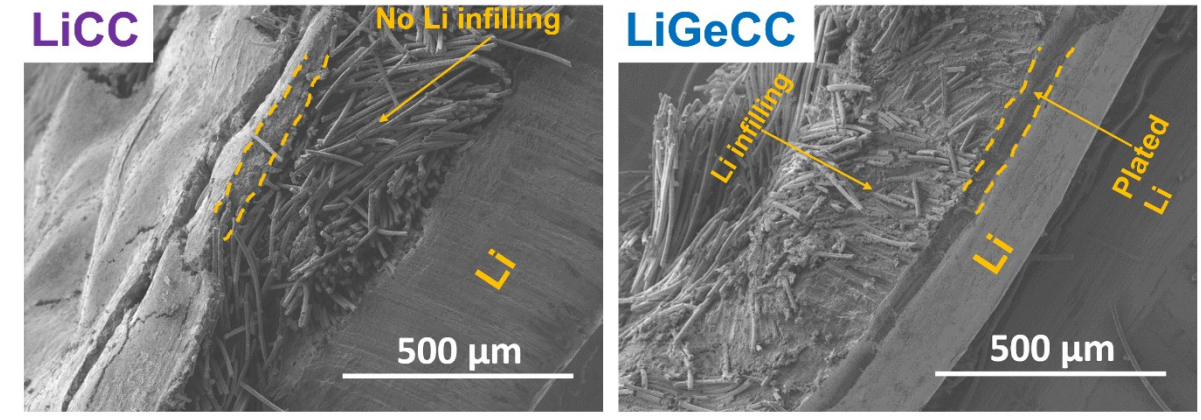

Figure S19. Comparison of cross-sectional SEM of LiCC and LiGeCC at 4 mAh cm^{-2} plating capacity after 100 cycles.

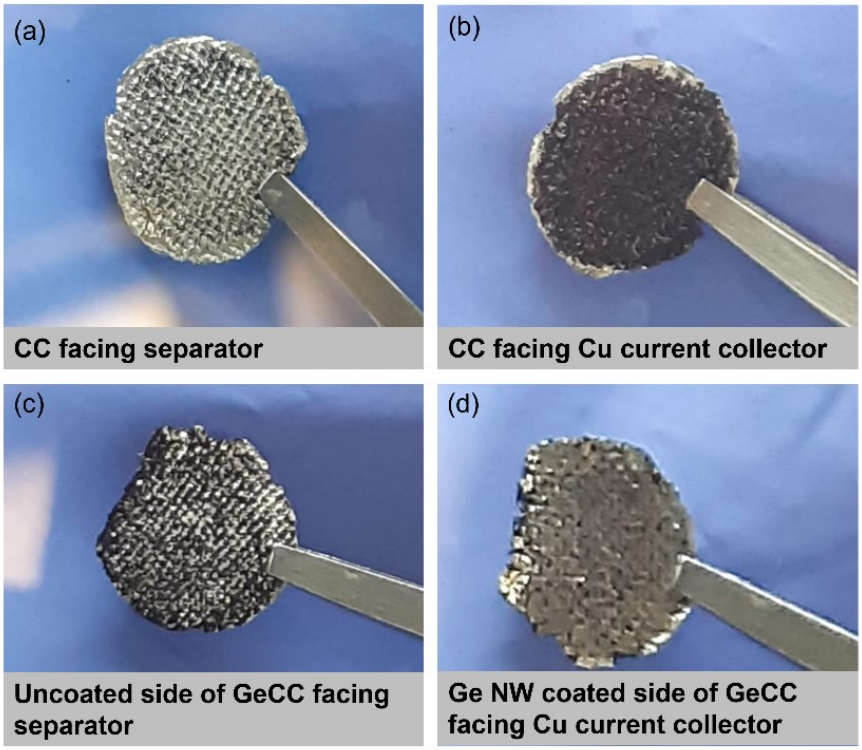

Figure S20. Li plating on CC (a) facing the separator and (b) facing the Cu current collector. Li plating on the GeCC (c) CC side facing the separator and (d) Ge NW side facing the Cu current collector. For both samples 4 mAh cm^{-2} Li was plated at a current density of 2 mA cm^{-2}.

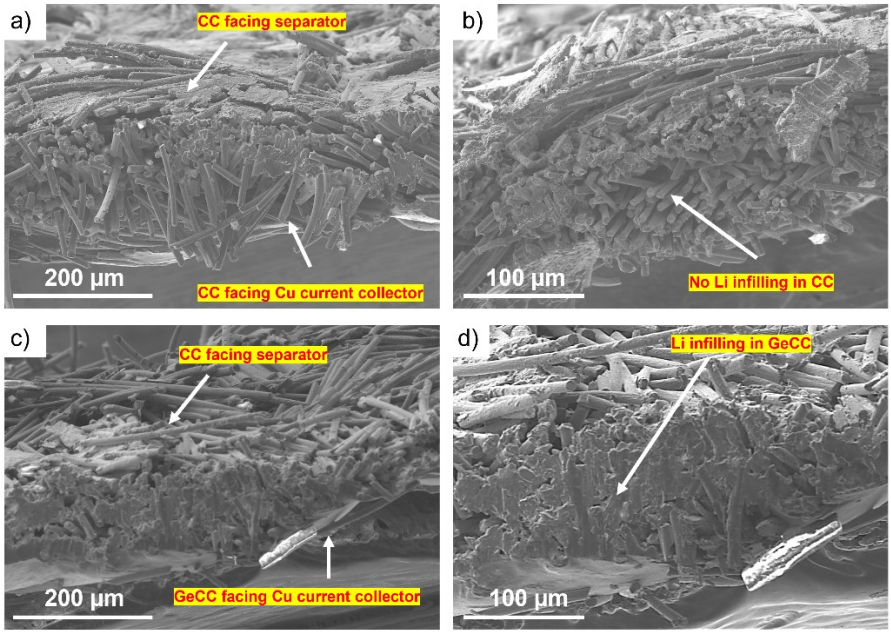

Figure S21. Cross-sectional SEM images of (a, b) CC and (c, d) GeCC as substrates after 4 mAh cm^{-2} Li plating in a Li vs. CC and Li vs. GeCC half-cell.

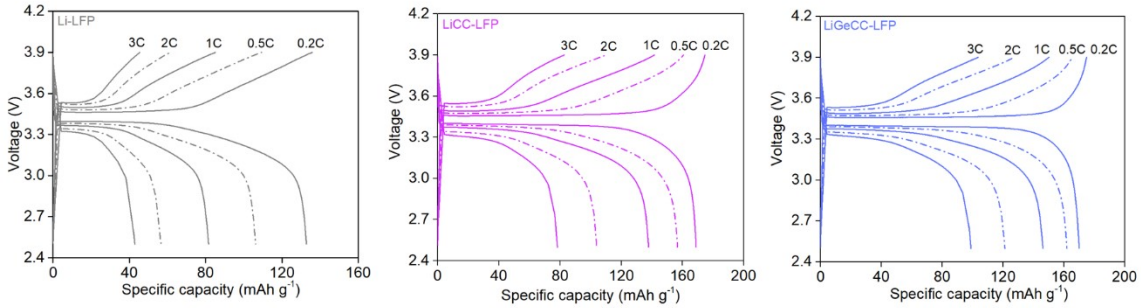

Figure S22. Voltage vs. Specific capacity plot of Li-LFP, LiCC-LFP and LiGeCC-LFP at various C-rates.

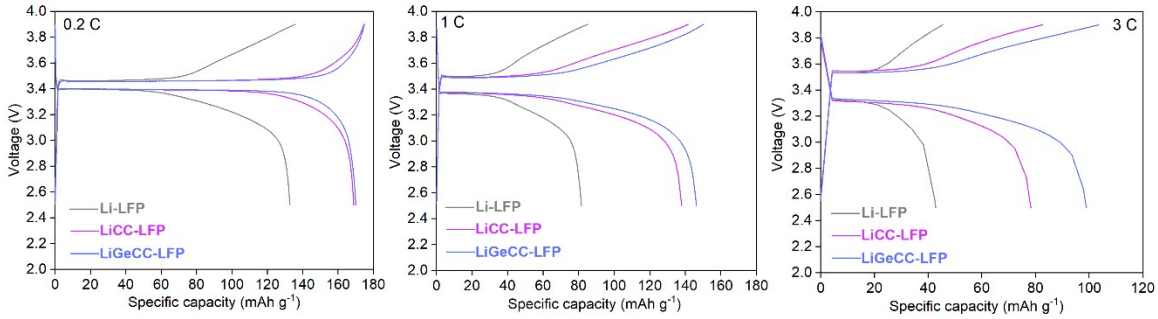

Figure S23. Comparison of voltage – specific capacity profile of Li-LFP, LiCC-LFP and LiGeCC-LFP at 0.2, 1 and 3 C.

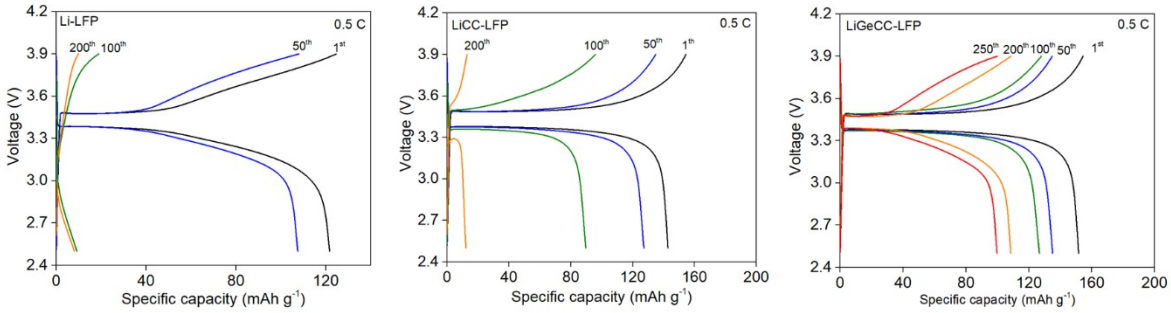

Figure S24. Voltage vs. Specific capacity plot of Li-LFP, LiCC-LFP and LiGeCC-LFP at various cycle no.

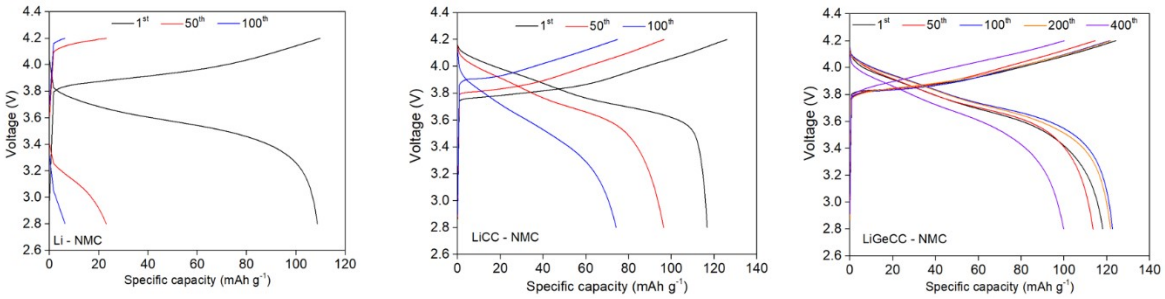

Figure S25. Voltage vs. Specific capacity plot of Li-NMC, LiCC-NMC and LiGeCC-NMC at various cycle no.

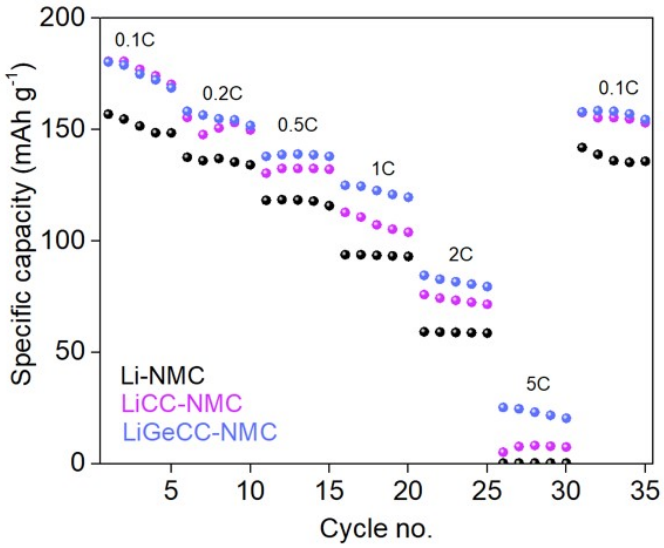

Figure S26. Rate capability performance of Li-LFP, LiCC-LFP and LiGeCC-LFP at various C-rates

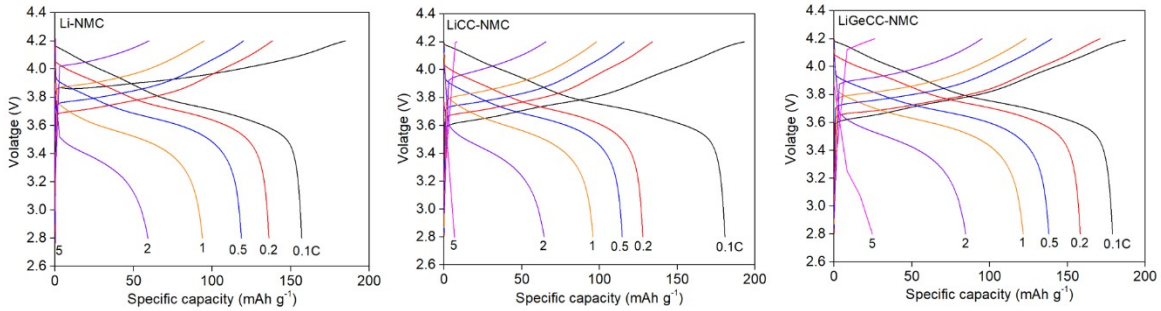

Figure S27. Voltage vs. Specific capacity plot of Li-NMC, LiCC-NMC and LiGeCC-NMC at various C-rates.

List of symbols

Capital letters

D	Diffusion coefficient
F	Faraday constant
M	Molar mass
$\vec{N}_{e,eff}$	Effective particle flux in the bulk electrolyte
R	Universal gas constant
T	Temperature
U_0	Open circuit potential (OCV)

Lowercase letters

a	Specific surface area for Li plating
a_0	Specific surface area of the host material (CC)
c	Concentration
f_{thermo}	Thermodynamic factor
i	Applied current density during galvanostatic cycling
i_0	Amplitude of the Butler-Volmer equation (exchange current density)
i_{se}	Current density at the electrode-electrolyte interface
$\vec{j}_{e,eff}$	Effective ionic current in the bulk electrolyte
$\vec{j}_s$	Electric current in the bulk (solid) electrode
k_{BV}	Reaction rate constant of the Butler-Volmer equation
n	Amount of substance

t	Time
t_+	Transference number

Greek letters

α	Symmetry factor of the Butler-Volmer equation
β	Bruggeman coefficient
ε_e	Volume fraction of the electrolyte
$\varepsilon_{e,0}$	Porosity of electrode or separator
ε_{Li}	Volume fraction of plated Li
$\varepsilon_{Li,eff}$	Effective volume fraction of plated Li
$\varepsilon_{Li,ref}$	Reference volume fraction of plated Li corresponding to a fully covered surface of the electrode / host material (CC)
η	Overpotential of the electrochemical reaction
η_{nuc}	Nucleation Overpotential
Θ	Fractional coverage of the electrode surface with Li metal
κ	Ionic conductivity of the electrolyte
ρ	Density
σ	Electronic conductivity of the electrode
τ	Tortuosity
φ_e	Electrochemical potential of the electrolyte
Φ_s	Electric potential of the electrode

Subscripts s, e and Li indicate a quantity of the solid (host) electrode, the electrolyte and the plated Li respectively.

References

1 R. Richter, J. Häcker, Z. Zhao-Karger, T. Danner, N. Wagner, M. Fichtner, K. A. Friedrich and A. Latz, ACS Appl Energy Mater, 2020, 3, 8457–8474.

2 D. Zhou, A. Tkacheva, X. Tang, B. Sun, D. Shanmukaraj, P. Li, M. Armand and G. Wang, Angewandte Chemie International Edition, 2019, 58, 6001–6006.

3 M. Safari, C. Y. Kwok and L. F. Nazar, ACS Cent Sci, 2016, 2, 560–568.

4 C. von Lüders, J. Keil, M. Webersberger and A. Jossen, J Power Sources, 2019, 414, 41–47.

5 K. Yan, Z. Lu, H. W. Lee, F. Xiong, P. C. Hsu, Y. Li, J. Zhao, S. Chu and Y. Cui, Nat Energy, 2016, 1, 1–8.

6 P. Biswal, S. Stalin, A. Kludze, S. Choudhury and L. A. Archer, Nano Lett, 2019, 19, 8191–8200.

7 S. Hein, T. Danner and A. Latz, ACS Appl Energy Mater, 2020, 3, 8519–8531.

8 K. Xie, K. Yuan, K. Zhang, C. Shen, W. Lv, X. Liu, J. G. Wang and B. Wei, ACS Appl Mater Interfaces, 2017, 9, 4605–4613.

9 V. V. K. Lanjapalli, F. J. Lin, S. Liou, S. Hosseini, C. L. Huang, Y. S. Chen and Y. Y. Li, Electrochim Acta, 2022, 410, 139976.

10 H. Kim, Y. J. Gong, J. Yoo and Y. S. Kim, J Mater Chem A Mater, 2018, 6, 15540–15545.

11 Q. Li, S. Zhu and Y. Lu, Adv Funct Mater, 2017, 27, 1606422.

12 Y. Zhou, Y. Han, H. Zhang, D. Sui, Z. Sun, P. Xiao, X. Wang, Y. Ma and Y. Chen, Energy Storage Mater, 2018, 14, 222–229.

13 Y. Chen, M. Yue, C. Liu, H. Zhang, Y. Yu, X. Li and H. Zhang, Adv Funct Mater, 2019, 29, 1806752.

14 J. Fan, Y. Tian and C. Wang, Dalton Transactions, 2022, 51, 4275–4283.

15 H. Zhang, X. Liao, Y. Guan, Y. Xiang, M. Li, W. Zhang, X. Zhu, H. Ming, L. Lu, J. Qiu, Y. Huang, G. Cao, Y. Yang, L. Mai, Y. Zhao and H. Zhang, Nat Commun, 2018, 9, 1–11.

16 Y. Sun, C. Zhao, K. R. Adair, Y. Zhao, L. V. Goncharova, J. Liang, C. Wang, J. Li, R. Li, M. Cai, T. K. Sham and X. Sun, Energy Environ Sci, 2021, 14, 4085–4094.

17 S. Zhang, J. You, Z. He, J. Zhong, P. Zhang, Z. Yin, F. Pan, M. Ling, B. Zhang and Z. Lin, Adv Funct Mater, 2022, 32, 2200967.